JGR Space Physics

RESEARCH ARTICLE
10.1029/2018JA026309

Multi-Instrumental Observation of Storm-Induced Ionospheric Plasma Bubbles at Equatorial and Middle Latitudes

Iurii Cherniak[1,2], Irina Zakharenkova[2], and Sergey Sokolovsky[1]

[1]COSMIC Program Office, University Corporation for Atmospheric Research, Boulder, CO, USA, [2]Space Radio-Diagnostic Research Center, UWM, Olsztyn, Poland

Key Points:
- Prompt penetration electric field during June 2015 storm led to generation of large-scale plasma bubbles in the postsunset sector
- Affected area has a large longitudinal range of ~100 degrees in American sector and a localized zone of ~20 degrees in longitude in African sector
- Plasma depletions of equatorial origin were registered at midlatitudes (30–40 deg MLAT) of African and American longitudinal sectors

Supporting Information:
- Supporting Information S1
- Movie S1
- Movie S2

Correspondence to:
I. Cherniak,
iurii@ucar.edu

Citation:
Cherniak, I., Zakharenkova, I., & Sokolovsky, S. (2019). Multi-instrumental observation of storm-induced ionospheric plasma bubbles at equatorial and middle latitudes. *Journal of Geophysical Research: Space Physics*, *124*, 1491–1508. https://doi.org/10.1029/2018JA026309

Received 18 NOV 2018
Accepted 16 FEB 2019
Accepted article online 22 FEB 2019
Published online 15 MAR 2019

Abstract June solstice is considered as a period with the lowest probability to observe typical equatorial plasma bubbles (EPBs) in the postsunset period. The severe geomagnetic storm on 22–23 June 2015 has drastically changed the situation. Penetrating electric fields associated with a long-lasting southward IMF support favorable conditions for postsunset EPBs generation in the dusk equatorial ionosphere for several hours. As a result, the storm-induced EPBs were progressively developed over a great longitudinal range following the sunset terminator. The affected area has a large longitudinal range of ~100° in the American sector and a rather localized zone of ~20° in longitude in the African sector. Plasma depletions of equatorial origin were registered at midlatitudes (30°–40° magnetic latitude) of both hemispheres in the African and American longitudinal sectors. We examine global features of the large-scale plasma depletion by using a combination of ground-based and space-borne measurements—ground-based Global Positioning System/Global Navigation Satellite System (GPS/GNSS) networks, Constellation Observing System for Meteorology, Ionosphere, and Climate (COSMIC) GPS Radio Occultation (RO), Swarm upward looking GPS data, and in situ plasma density observations provided by Swarm, Communications/Navigation Outage Forecasting System (C/NOFS), and Defense Meteorological Satellite Program (DMSP) missions. Joint analysis of the satellite observations revealed that these storm-induced EPBs structures had extended over 500 km in altitude, at least from ~350 to ~850 km. These irregularities caused strong amplitude and phase scintillations of GPS/GNSS signals for ground-based and space-borne (COSMIC RO) measurements and seriously affected performance of navigation-based services.

1. Introduction

Equatorial plasma bubbles (EPBs) represent a typical postsunset phenomenon in the form of plasma density depletions of different scales (50–1,000 km) observed in the equatorial ionosphere within a narrow band of ±20° magnetic latitude (MLAT) and covered a broad range of altitudes from the bottomside ionosphere up to 1,000 km (Kelley, 1989; Woodman & La Hoz, 1976). The ionospheric turbulences related to the EPBs development can severely disrupt the transionospheric radio wave propagation channel by affecting both amplitude and phase of the radio signal, which are called scintillations. On the one hand, it can lead to a severe degradation or even outage of safety-of-life systems performance, in particular Global Navigation Satellite System (GNSS)-based ones (e.g., Basu et al., 2008; Doherty et al., 2004; Roy et al., 2013). On the other hand, we can use GNSS as a precise tool for detection and continuous monitoring of ionospheric plasma irregularities on global or regional scales (Aarons, 1997; Cherniak et al., 2014; Cherniak & Zakharenkova, 2016; Jakowski et al., 2012; Pi et al., 1997; Shagimuratov et al., 2012; Valladares et al., 2004).

The EPBs are considered as the most severe plasma density perturbations that developed primarily in the equatorial ionosphere during both quiet time and disturbed conditions. The second area with strong ionospheric perturbations locates at high latitudes above ~65° MLAT, which includes auroral and polar cap regions. Here, severe ionospheric irregularities occur primarily during geomagnetic disturbances. During quiet time, the ionosphere at middle latitude is considered being free from ionospheric irregularities or plasma density gradients apart from signatures of the main ionospheric trough. However, development of strong geomagnetic disturbances leads to a wide expansion of the auroral irregularities region in an equatorward direction. Observations of auroral irregularities at midlatitudes (40–45°N) were reported in Europe during the Halloween 2003 superstorm (Jakowski et al., 2008) and in Northern America for the St. Patrick's Day 2015 storm (Cherniak et al., 2015). In even more rare conditions, the midlatitude

ionosphere can be affected by ionospheric irregularities expanding in a poleward direction from the equatorial region. In such cases, the EPB-related ionospheric plasma density perturbations can be registered at midlatitudes.

With development of a geomagnetic storm, perturbed electric fields can arise at the equator from prompt penetrating electric field (PPEF) and/or electric field due to ionospheric disturbance dynamo. When the storm-induced electric fields occur in the dusk sector, they superimpose on the normal prereversal enhancement (PRE) and can lead to the suppression of postsunset EPBs occurrence (Aarons, 1991; Fejer et al., 1999) or initiate more dramatic development of EPBs due to much larger uplift of the ionosphere to high altitudes where the Rayleigh-Taylor instability (RTI) growth rate is maximized (e.g., Abdu et al., 1995; Basu et al., 2001, 2007; Ossakow, 1981). Using the Defense Meteorological Satellite Program (DMSP) in situ measurements of ion density, Basu et al. (2001) reported the presence of the severe ion density bite-outs extending in latitudes by ~30° (±10–15° around the magnetic equator) in South Atlantic during the 15 July 2000 storm, which indicated that the ionospheric *F* region was uplifted up to the DMSP altitude (~840 km). Severe plasma bite-outs can significantly enlarge a latitudinal extent of the storm-induced EPBs to both sides from the magnetic equator. Thus, Ma and Maruyama (2006) reported one of the first observations of the postsunset plasma bubbles at midlatitudes (Japanese sector). During the 12 February 2000 geomagnetic storm, the plasma bubbles appeared in the midlatitudinal sector ~30–34°N (~31° MLAT), ~130–134°E. The EPB-related plasma depletions were registered at midlatitudes (up to ~46° MLAT) by the DMSP observations during the October 2003 superstorm (Huang et al., 2007). Using the ground-based GNSS measurements (TEC (total electron content) and ROTI (rate of TEC index)) and in situ data of plasma density from Swarm and DMSP satellites, Cherniak and Zakharenkova (2016) reported an occurrence of the plasma bubbles in Europe for the June 2015 storm. Plasma depletions were observed in the sector ~40–45°N (~35–40°N MLAT), ~0–35°E over 8 hr; they were related to the plasma bite-out in the dusk sector over the West African longitudes. Recently, Aa et al. (2018) reported the midlatitude postsunset EPBs observations over China for the September 2017 storm. The ionospheric irregularities were registered for ~5 hr at latitudes of 20–50°N (up to 45° MLAT).

During severe geomagnetic storms, strong ionospheric plasma irregularities are considered as critical threats to transionospheric radio communication links and can led to a severe performance degradation/outage of the GNSS-based systems, for example, Satellite-Based Augmentation System (SBAS) signals. In particular, Doherty et al. (2004) investigated the performance degradation of the American Wide Area Augmentation System (WAAS) for the superstorm in 2003, Cherniak and Zakharenkova (2016) reported noticeable degradation of positioning accuracy of the European system European Geostationary Navigation Overlay Service (EGNOS) for the June 2015 storm. Thus, one of the most challenging and key tasks is to improve the current understanding of the ionospheric plasma irregularities morphology and spatiotemporal manifestation of the rarely expected ionospheric irregularities focusing on their dependences on geophysical factors. Another open question is how geomagnetic storms affect the plasma bubbles generation and lead to differences from the EPB occurrence climatology. The plasma irregularities developing at high/middle and low latitudes have entirely different physical mechanisms of their generation and further evolution. Approaches based on radio waves propagation throughout these structures can effectively detect all of them. The aim of this study is to analyze the main features of the ionospheric plasma irregularities development at midlatitudes under severe geomagnetic storm conditions and to estimate physical drivers leading to the structures generation.

We analyze an occurrence and evolution of the midlatitude plasma bubbles structures for the case of the June 2015 geomagnetic storm. This storm provides opportune circumstances for storm-induced EPBs development and a further EPBs expansion toward midlatitudes at two longitudinal zones—the American and European/African regions. We examine global features of the large-scale plasma depletion combining the multisite and multi-instrumental measurements: ground-based Global Positioning System/Global Navigation Satellite System (GPS/GNSS) networks, Constellation Observing System for Meteorology, Ionosphere, and Climate (COSMIC) GPS Radio Occultation (RO), Swarm GPS and in situ observations, and in situ data from onboard the Communications/Navigation Outage Forecasting System (C/NOFS) satellite and the Defense Meteorological Satellite Program (DMSP) F15 satellite. We investigated a relationship between the space weather drivers and processes of plasma irregularities development to reveal global drivers originated these processes.

We also demonstrate to which extent an integration of independent but compatible modern ground-based and space-borne observations can support investigations on the origin and dynamics of ionospheric plasma irregularities in view of the forthcoming COSMIC-2 mission.

2. Database

2.1. Ground-Based GNSS Measurements

To detect that signatures of the plasma density perturbations accompanied the EPBs development, we analyze raw GNSS observations from ~6,400 ground-based stations worldwide. Moreover, near 3,500 stations received navigation signals not only from United State's GPS but from Russia's GLONASS (In Russian: GLObalnaya NAvigazionnaya Sputnikovaya Sistema) satellites too. GLONASS satellites operates in three near-circular orbits inclined at ~64.8°, about 10° greater than orbits of GPS and Galileo systems, providing a much better coverage at high latitudes. Joint use of GPS and GLONASS allows to augment an amount of accessible observations at all latitudes and gives an opportunity to detect the ionospheric plasma density irregularities with a much higher spatial and temporal resolution. We should note that such multiconstellation, multi-GNSS approach is a very perspective one, and it will be applied in the next generation of the COSMIC-2 mission. Each of the six COSMIC-2 satellites will have a "Tri-GNSS" receiver allowing to track simultaneously GPS, GLONASS, and Galileo navigational signals.

Ionospheric irregularities lead to rapid fluctuations of amplitude and phase of the navigation radio signal. To characterize the phase fluctuation degree, it is used the GPS-based index—ROTI, proposed by Pi et al. (1997). ROTI is calculated as a standard deviation of time differential TEC in 5 min. ROTI expresses sharpness of the GPS phase fluctuations caused by ionospheric irregularities and by strong spatial gradients of TEC. We augmented the common GPS-based data set through the joint GPS&GLONASS data processing. We explained in detail the GPS&GLONASS data processing and ROTI calculation in Zakharenkova et al. (2016a), Cherniak and Zakharenkova (2017), and Cherniak et al. (2018). First, the ROTI values were calculated for every passage of GPS and GLONASS satellites (elevation above 20°) over a GNSS station. Second, the multisite ROTI values were binned into 0.5° latitude-longitude grid to generate global ROTI maps of 15-min interval and high spatial resolution.

2.2. Space-Borne GPS Measurements: COSMIC Mission

Another effective technique for ionosphere structure research uses the trainsionospheric radio waves propagation, and it was successfully implemented by the COSMIC mission. That 10+ years mission still operates and provides valuable data both for lower and upper atmosphere investigations. The six COSMIC satellites operated in six circular orbits inclined at ~72° with an altitude of 700–800 km. The satellites provided several types of measurements, including GPS-based RO measurements for probing the Earth's ionosphere and atmosphere. For the considered period, there were available data from four COSMIC satellites—FM1, FM2, FM5, and FM6. In this study, we use several types of the COSMIC RO measurements. First, we use the main COSMIC RO ionospheric product "ionPrf"—ionospheric electron density profiles—to analyze the storm-induced changes in the profile shape and an altitude distribution of ionospheric irregularities.

Second, additionally to the COSMIC ionospheric electron density profiles, this space-borne GPS experiment provides another GPS RO product—the S4-index. While the ROTI index is considered as a measure of the GPS signal phase fluctuations, the S4-index serves as a measure of the GPS signal amplitude fluctuations (Basu & Basu, 1989). The amplitude scintillation index, S4, is determined by a ratio of the standard deviation of signal intensity to the average signal intensity. As known, the amplitude scintillations are the most prominent near the geomagnetic equator and they regularly appear in the postsunset hours in a direct relation to postsunset EPBs development. We should note an important difference between high- and low-latitude irregularities—while intense EPBs can lead to large values of both the phase scintillations (seen in ROTI) and amplitude scintillations (seen in S4) of GPS signals, the intense high-latitude irregularities are characterized by stronger phase fluctuations and rather weak amplitude scintillations (Jiao et al., 2013; Prikryl et al., 2010; Skone et al., 2008). Onboard the COSMIC satellites, intensity of amplitude fluctuations are determined from raw L1 amplitude measurements (signal-to-noise ratio, SNR) of 50-Hz rate and then these estimates are downstreamed with 1 Hz temporal resolution. In the "scnLv1" product, each file contains information about the S4 index values, SNR on the GPS L1 frequency, minimum (S4min) and maximum (S4max) values of the S4 index, tangent point location (latitude, longitude, and altitude), universal time

(UT), and position of the COSMIC and GPS satellites making the RO observation. Since S4 index is a very sensitive indicator of the GPS signal amplitude scintillations, the COSMIC S4-index product allows detecting the geographical, altitudinal, and temporal allocation of the ionospheric irregularities on a global scale.

Third, we apply back propagation (BP) technique for an approximate localization of the ionospheric irregularities that cause scintillation of RO signals. The BP uses the RO signal's phase and amplitude measured on receiver trajectory as the boundary condition for propagation of electromagnetic field back to transmitter, thus solving for the effects of diffraction and multipath propagation in free space (Hinson et al., 1998). The BP was used to investigate the sporadic Es layer (Gorbunov et al., 2002) and to localize high-altitude ionospheric irregularities (Sokolovskiy et al., 2002). In order to be "localizable" along the line GPS-LEO (low Earth orbit), the irregularities must satisfy two conditions. First, the irregularities must be anisotropic (elongated) with maximum scales much larger than the Fresnel zone. This is necessary because the electromagnetic field is observed on 1-D trajectory and this allows to reduce the BP problem to 2-D in the plane normal to expected elongation direction of the irregularities (for isotropic, 3-D, irregularities, the wave propagation problem with 1-D boundary condition is underdetermined). Commonly, the ionospheric irregularities above the sporadic *E* layer are elongated along the magnetic field. Second, the irregularities must occupy a volume where they only induce the phase modulation, while the amplitude modulation inside the volume is small (may become large far away from the volume). This allows to localize the irregularities by detecting the minimum of root-mean-square (RMS) fluctuation of the BP amplitude. Behind the volume with irregularities (closer to transmitter), the amplitude fluctuation increases again in the BP field (which is different from the true incident field). In this study, related to low latitude and midlatitude irregularities, we use the assumption that magnetic field lines and thus the direction of elongation of irregularities are approximately horizontal (this assumption introduces certain localization errors which are neglected in this study).

2.3. Space-Borne In Situ Measurements

To determine the vertical extent of the ionospheric irregularities, we used in situ plasma probe measurements onboard several LEO satellites. First, we analyzed observations provided by the Swarm mission of three satellites—Swarm Alpha (A), Bravo (B), and Charlie (C) (hereafter called SWA, SWB, and SWC)—that operate at polar orbits of ~88° inclination. The satellite tandem (SWA&SWC) flies side by side (~1°) at height of ~465 km and the upper satellite (SWB)—at height of ~515 km. As of 22 June 2015, the local times of the ascending and descending nodes are ~10.9 and ~22.9 LT for SWA&SWC and ~12.9 and ~0.9 LT for SWB. Two Langmuir probes onboard each satellite provide 1-Hz measurements of in situ electron density (Ne).

Second, we used observations provided by the C/NOFS satellite flying with a low orbit inclination of 13°. As of June 2015, the C/NOFS elliptical orbit was decayed to ~330 × 450-km altitude. We analyzed the in situ ion density (Ni) measurements provided by the IVM (Ion Velocity Meter) instrument of the C/NOFS CINDI (Coupled Ion Neutral Dynamics Investigation) payload.

Third, the in situ ion density (Ni) data measured at ~850 km by the DMSP F15 satellite were also employed in this study. As of 22 June 2015, the local times of the ascending and descending nodes were ~15 and ~3 LT for the F15 satellite.

We should note that both GNSS-based and in situ observations have specific limitations. The ground-based GNSS and LEO GPS RO measurements provide a two-dimensional (2-D) snapshot of ionospheric plasma structures: 2-D latitude/longitude distribution (single layer maps) from the ground-based data and altitudinal electron density profiles from the COSMIC RO measurements. The in situ plasma probe measurements represent only 1-D horizontal slices of ionospheric plasma structures at satellite height.

3. The 22–23 June 2015 Geomagnetic Storm: Space Weather Conditions.

On 21–22 June 2015, two moderate and one giant coronal mass ejections (CMEs) reached the Earth magnetosphere and led to an occurrence of a severe geomagnetic storm (e.g., Augusto et al., 2018; NOAA Space Weather Highlights, 2019; Reiff et al., 2016). Figure 1 illustrates the space weather conditions for 21–23 June 2015. The first CME with Vsw ~ 350 km/s and the Psw ~ 13 nPa led to the first sudden storm commencement (SSC) registered at 16:44 UT on 21 June 2015 and the SYM-H index rose to ~45 nT. Further, the interplanetary magnetic field (IMF) vertical component Bz started to oscillate. The second SSC was at

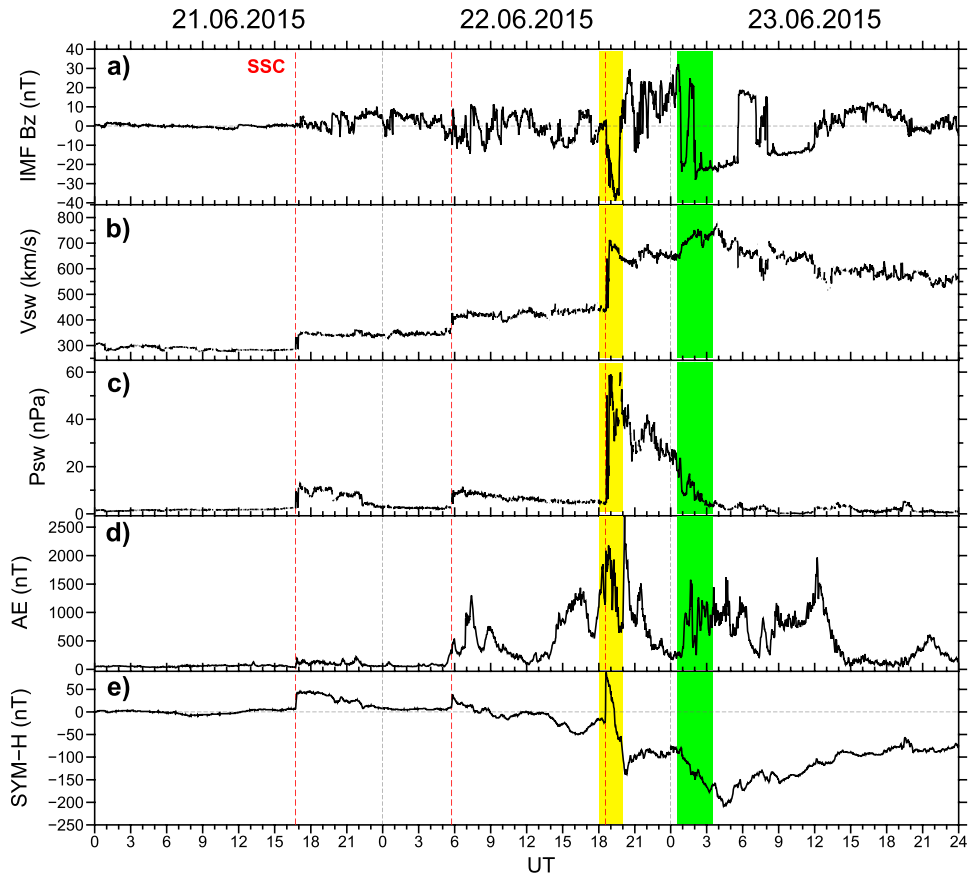

Figure 1. (a) Interplanetary magnetic field (IMF) Bz component, (b) velocity, and (c) dynamic pressure of the solar wind, (d) auroral electrojet index AE, and (e) SYM-H index during 21–23 June 2015. The red dotted lines show the three sudden storm commencement (SSC) moments. The yellow and green bars indicate temporal intervals for two events with plasma bite-outs and strong equatorial plasma bubbles development.

~05:45 UT on 22 June 2015. The Psw rose to ~10 nPa with Vsw ~ 420 km/s and the IMF Bz excursed southward. At that time, the AE (auroral electrojet) index increased to ~530 nT, the second AE peak of ~1,300 nT was registered at ~07:25 UT. The third SSC was registered at ~18:33 UT on 22 June 2015. Here, an interplanetary shock arrived with Vsw ~ 710 km/s and the Psw ~ 65 nPa. At that time (~18:38 UT), the IMF Bz excursed sharply southward, reached a minimum value of −39 nT at ~19:23 UT. After the third SSC, the SYM-H increased to +88 nT at 18:37 UT. Further, the SYM-H index decreased abruptly to −139 nT at 20:17 UT; thus, the rate of Dst change was −130 nT/hr. On 23 June 2015, two rapid southward turns of the IMF Bz occurred. The first one was a turn from +32 nT at 0:39 UT to −24 nT at 0:55 UT, the IMF Bz remained southward 1:29 UT. Shortly afterward, the IMF Bz turned from +24 nT at 01:40 UT to −28 nT at 2:04 UT and remained directed southward for several hours till ~05:40 UT. During this period, the second main phase of the storm developed and the SYM-H index dropped to a minimum of −208 nT at ~04:28 UT on 23 June 2015. Several AE peaks of ~1,000–2,500 nT were registered till 14 UT of 23 June 2015.

4. Results and Discussion

4.1. Global Overview of Plasma Irregularities Development During the Storm Time

According to climatological studies, the EPBs occurrence probability peak falls on equinoxes and its lowest values observed during June solstices (e.g., Burke et al., 2004). For the year 2015, Zakharenkova et al. (2016b) analyzed onboard GPS and in situ measurements from Swarm satellites and reported the lowest occurrence probability (less 10–15%) to observe postsunset EPBs for the June 2015 season. Did the strong geomagnetic storm change this situation?

We present an overview of the storm-induced ionospheric irregularities that appeared at midlatitudes during the June 2015 geomagnetic storm. We processed the ground-based GNSS observations and applied the GNSS ROTI mapping approach to detect and to geolocate plasma irregularities over the wide areas covered by the dense GNSS networks. Figure 2 presents series of the ROTI maps covering the American and Europe/Africa sectors for selected epochs on 22–23 June 2015 when the storm occurred. Supporting information (Movies S1 and S2) contains an entire 24-hr set of the ROTI maps with a 15-min rate for 22 and 23 June 2015.

Figure 2a shows the ROTI map for relatively quiet conditions between two SSC at ~03 UT on 22 June 2015. Here, we find only weak-to-moderate auroral ionospheric irregularities at high latitudes. In the equatorial region, we do not observe EPBs in the postsunset and nighttime period at the American and African longitudinal sectors; that is in well agreement with climatological results of very low occurrence probability of EPBs during the June solstice season. Figures 2b and 2c illustrate conditions for 8:30 UT and 15:30 UT corresponding two peaks of the AE index to ~1,000 nT after the second SSC. We can note an intensification of the auroral ionospheric irregularities over the northern polar cap.

The third SSC registered at ~18:33 UT on 22 June 2015 led to an immediate AE index increase to ~2,000 nT. Figure 2d shows a response of the high-latitude ionosphere to the auroral activity increase in the form of an expansion of the auroral oval with intense ionospheric irregularities. The IMF Bz turned southward and it reached −39 nT. The SYM-H index was increased to +88 nT and then dropped rapidly to −139 nT at 20:17 UT; thus, the rate of its change was −130 nT/hr. When a sudden intensification of the ring current occurs leading to the SYM-H decreases at a rate exceeding −50 nT/hr, the PPEF from high latitudes causes formation of the ionospheric electron density irregularities in the equatorial region (e.g., Basu et al., 2001, 2005). In the dusk sector, the PPEF adding to the postsunset eastward E field can cause a rapid uplift of the ionosphere and sets off plasma instabilities to form bubbles or bite-outs. At that time, the solar terminator just crossed the western part of Africa and here occurred the most favorable conditions for superimposing PPEF to the normal PRE. Figure 2e shows a further expansion of the oval-like zone with intense auroral irregularities (ROTI > 0.8–1 TECU/min) at high latitudes and appearance of the ionospheric irregularities at equatorial latitudes of Western Africa. At ~20 UT on 22 June 2015 (Figure 2f), an intensity of the EPBs at that zone was decreased while signatures of three elongated structures appeared near 30–40°N over the southern Europe and northern Africa sector. It is clearly seen that these structures have elongated in the meridional direction and they did not connect to auroral oval zone with plasma density irregularities of the auroral particles precipitation origin. The ionospheric irregularities within these three structures remained very intense and persisted for several hours (Figures 2f–2m), while auroral irregularities became weaker (Figures 2i–2k) during an AE drop to ~500 nT.

On 23 June 2015, two rapid southward turns of the IMF Bz occurred at ~0:39 UT and at ~01:40 UT, the AE index again rose to ~1,200–1,500 nT. As a result, the auroral irregularities oval characterized by a strong ROTI enhancement was clearly recognized at high latitudes (Figures 2l–2n). At that time, the ionospheric irregularities related to the storm-induced EPBs became much weaker within the European-African sector and further disappeared. Totally, these structures persisted for ~8 hr from 19 UT till 03 UT. But, at ~03 UT on 23 June 2015, the ionospheric irregularities appeared at equatorial latitudes in the American sector (Figure 2m) and they were further extended toward midlatitudes of both hemispheres (Figures 2n–2t). These structures were also inclined along the magnetic field lines in the meridional direction, similar to the structures developed a few hours earlier over the European-African sector. These irregularities persisted within this sector from ~03 UT to 09 UT on 23 June 2015.

Figure 3 shows a series of the 2-hr global maps of ionospheric irregularities as specified by the COSMIC RO S4 index product. We considered only RO profiles with a perigee point above 200 km to avoid capturing the ionospheric irregularities related with the sporadic E layer. At 16–18 UT (Figure 3a), the S4 index map shows a map with an absence of significant amplitude scintillations. The S4 index map for 18–20 UT (Figure 3b) revealed one noticeable event with S4 = 0.6 at 19:50 UT over the Western coast of Africa, exactly over the region where the storm-induced EPBs were detected by the ground-based GPS observations (cf. Figure 2e and 2f). During 20–22 UT (Figure 3c), a favorable location of the COSMIC satellites provided us more observation over the European-African sector, where the ionospheric irregularities caused the very strong amplitude scintillations (S4 ~ 1.0–1.8). For the time interval of 22–02 UT (Figures 3d and 3e), an intensity of the amplitude scintillations caused by the EPBs decreased practically to the prestorm conditions. But at 02–04

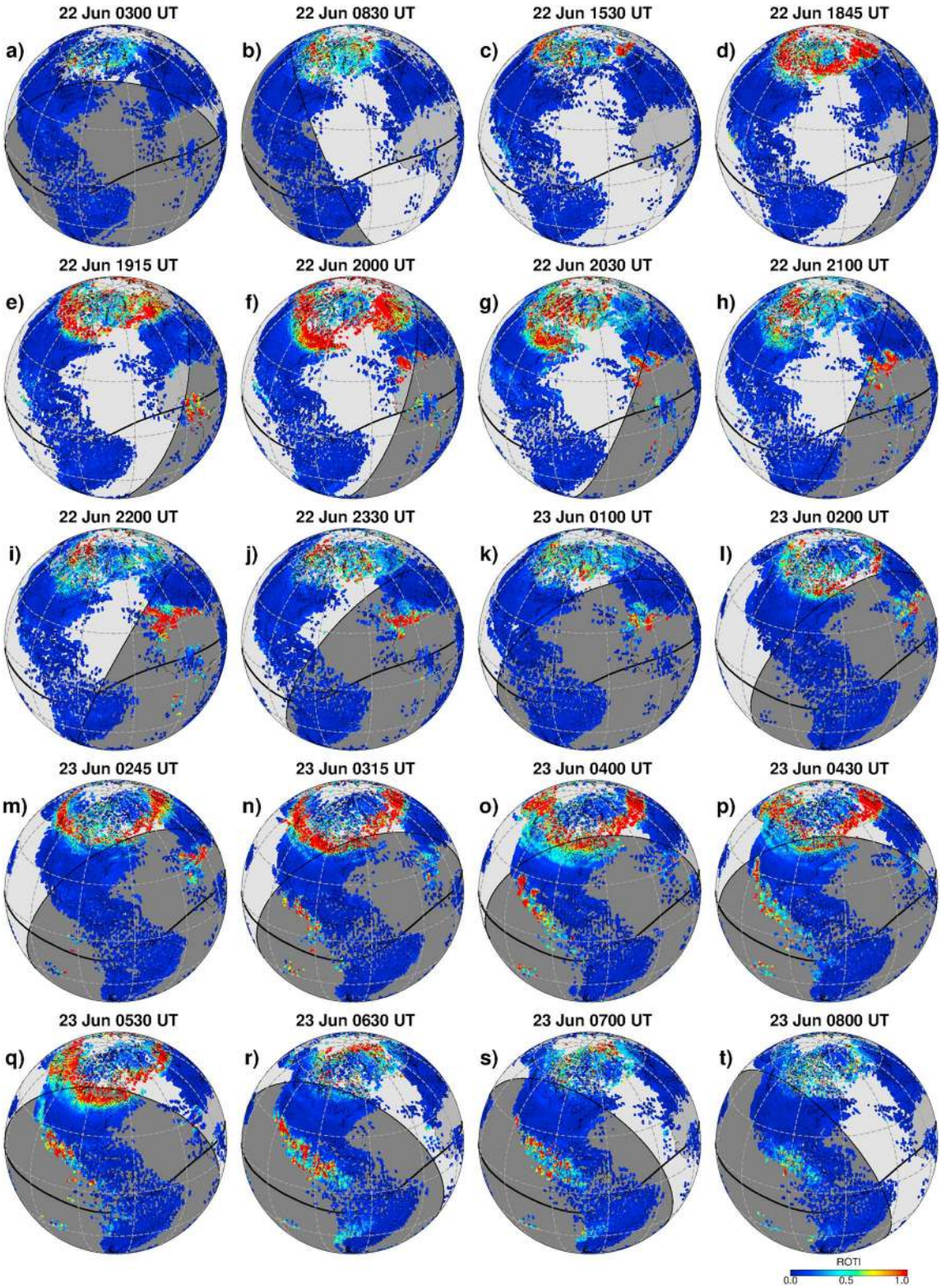

Figure 2. (a–t) GPS/GLONASS ROTI maps for specific times on 22–23 June 2015. The thick black line marks the geomagnetic equator. Gray shading shows nighttime and the solar terminator at 100-km altitude. High ROTI values (intense red color) depict severe ionospheric irregularities of equatorial and auroral origin. GPS = Global Positioning System; GLONASS = Russian Global Navigation Satellite System; ROTI = rate of TEC index.

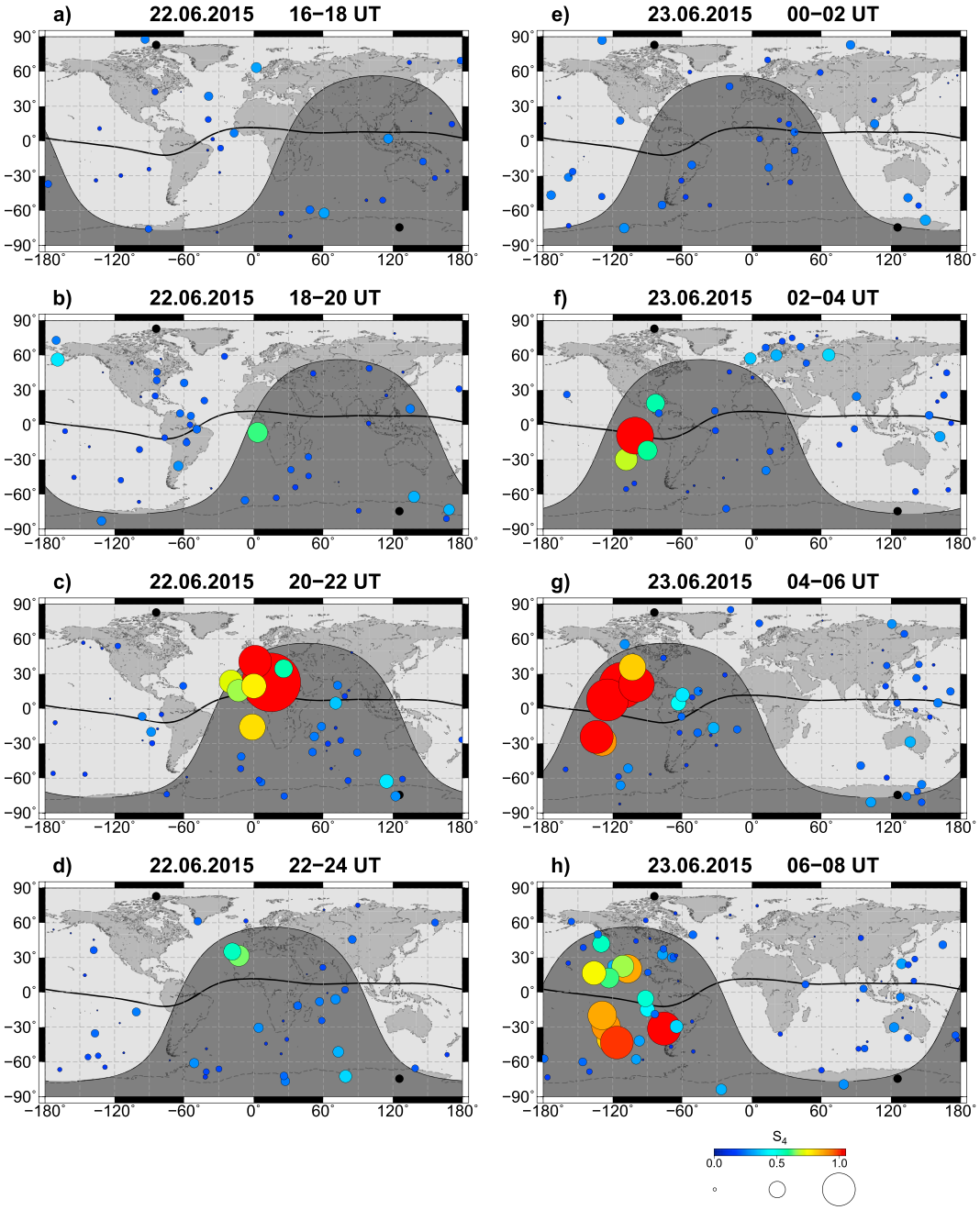

Figure 3. (a–h) The 2-hr global maps of ionospheric irregularities as specified by the COSMIC RO S4 index for 22–23 June 2015. The circle size is proportional to the S4 magnitude. Gray shading shows nighttime and the solar terminator at 100-km altitude.

UT on 23 June 2015 (Figure 3f), the S4 index map revealed a new area with the intense equatorial ionospheric irregularities at the American sector near 100–120°W. For the next hours from 04 UT to 08 UT (Figures 3g and 3h), this zone was significantly enlarged over the Pacific Ocean and the amplitude scintillations reached the value of S4 ~ 1.0–1.4.

As known, amplitude scintillations of navigation signals are produced by rapid changes of the refractive index due to different scale ionospheric plasma turbulences and inhomogeneities. These scintillations are referred primarily to the equatorial ionosphere where EPBs are typically developed (Basu et al., 1976). When size of these tiny plasma structures inside the EPBs is about the first Fresnel zone, they cause

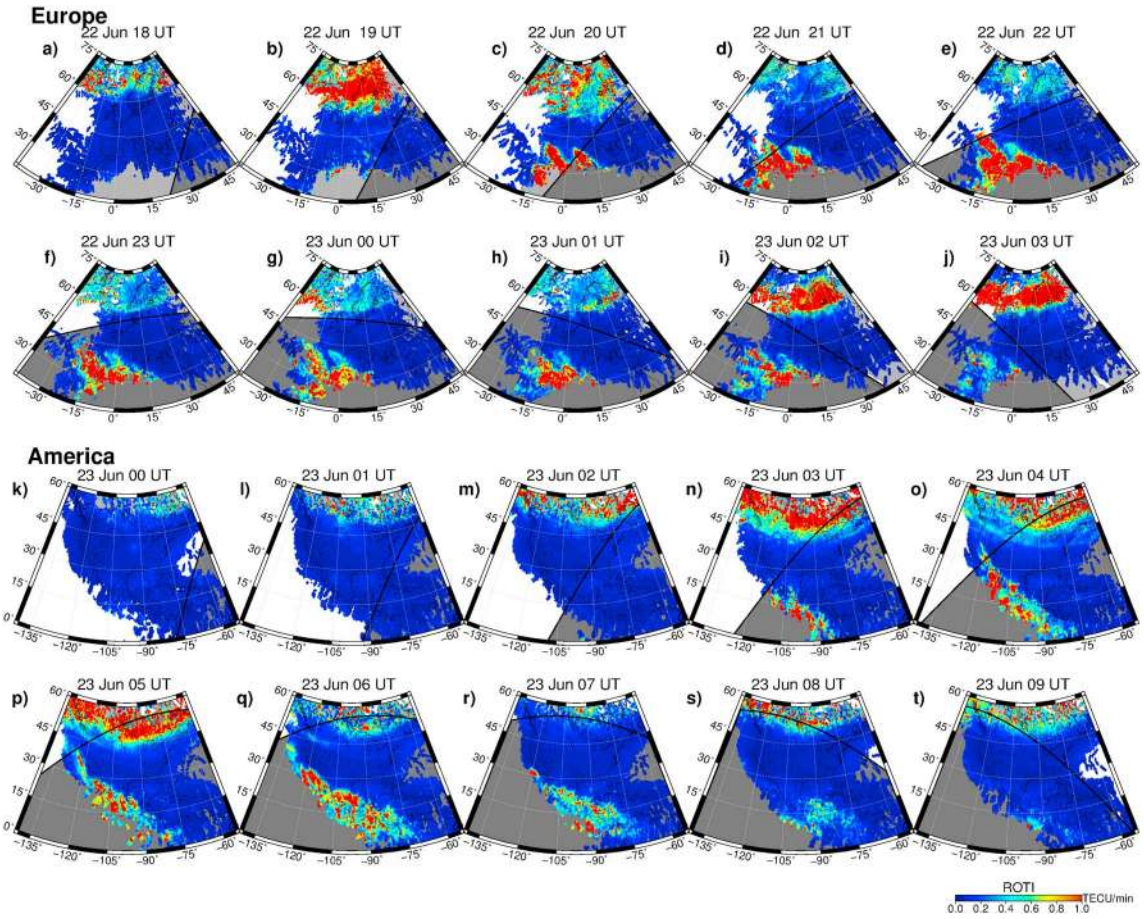

Figure 4. High-resolution hourly ROTI maps for (a–j) Europe and (k–t) American regions for 22–23 June 2015. Gray shading shows nighttime and the solar terminator at 100-km altitude.

amplitude scintillations of propagated radio signals. For the GNSS system frequencies, this size is about few hundreds of meters.

Moreover, these highly intense irregularities lead to the EGNOS performance degradation in Europe. Positioning accuracy was decreased up to 10 times from nominal (Cherniak & Zakharenkova, 2016). Over southern Europe and northern Africa regions, this degradation was essentially larger than more expected degradation usually observed at auroral latitudes during geomagnetic storms.

4.2. Development of the Ionospheric Plasma Irregularities in the European and American Sectors

Figures 4a–4j show a series of the detailed ROTI maps over the European region from 18 UT on 22 June 2015 to 03 UT on 23 June 2015. For 18–19 UT, the plasma irregularities prevailed at subauroral latitudes. This period was characterized by a high auroral activity with the AE index of ~2,000 nT (see Figure 1d). Starting from 20 UT (Figure 4c), a new zone with much stronger irregularities expanded from the subequatorial region toward European midlatitudes. We found no relationship or interconnection between the auroral irregularities zone, and this new zone appeared over the southern part of Europe. Besides, an intensity of the southern ionospheric irregularities remained high even when the auroral irregularities zone was significantly reduced at high latitudes (Figures 4d–4h). This southern zone with strong plasma irregularities persisted over 8 hr and covered a large area from ~30–40°N to ~20°W–10°E with ~30° extent in the meridional direction. The ROTI maps revealed clearly three elongated large-scale structures. These large-scale structures showed a slow motion in the northwestern direction and appeared within 40–45°N latitudes in geographical and 35–41°N in geomagnetic domain. The strong plasma irregularities covered a large area over Mediterranean and southern Europe (Spain, Portuguese, and South France) and over the Atlantic Ocean

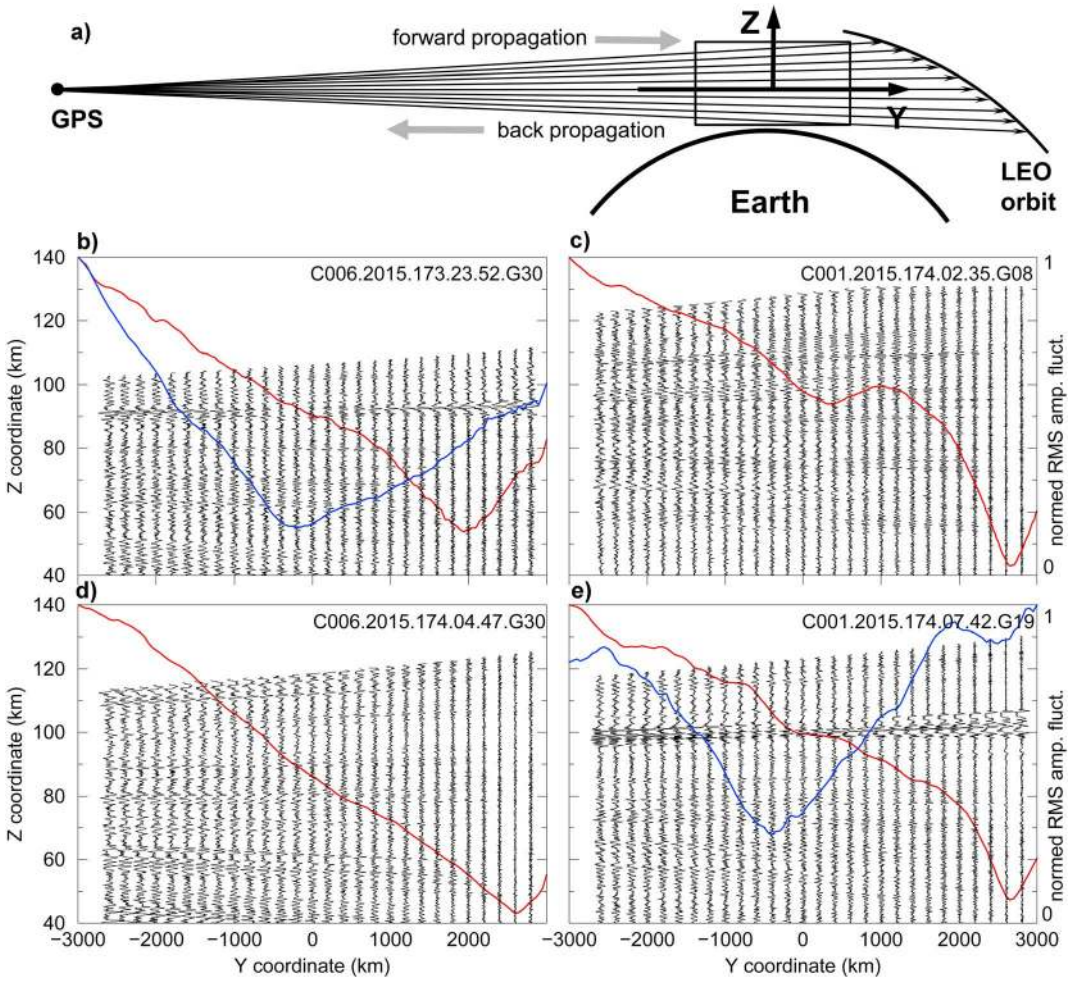

Figure 5. Signatures of ionospheric plasma irregularities in the 2-D back propagation (for details see text). (a) Schematic plot with the back propagation geometry. Geographical coordinates and heights of irregularities within the *F* layer, localized based on minimum of the rms of amplitude fluctuations are as follows: (b) 40°N, 24°W, ~350 km; (c) 21°N, 5°E, ~550 km; (d) 18°N, 109°E, ~550 km; (e) 2°N, 71°W, ~550 km. GPS = Global Positioning System; LEO = low Earth orbit.

(toward Canary Islands). We should note that a tilt of these structures projections against the geographical meridians was close to an angular difference between the geographical and geomagnetic meridians. It can be explained by an orientation of the plasma irregularities along the Earth's magnetic field lines.

In the American sector (Figures 4k–4t), the auroral irregularities appeared at ~01 UT and became the most intensive at ~03–05 UT on 23 June 2015. This time interval corresponded to a prolonged southward Bz and the AE index increase to ~1,000–1,500 nT. After 03 UT (Figure 4n), the plasma irregularities similar to the ones previously observed in Europe were detected over central America from Costa Rica to Mexico. During the next 2 hr, an area covered by the plasma irregularities was expended toward the continental United States, and plasma irregularities appeared even over California. In fact, plasma irregularities of equatorial origin reached ~40°N (50° MLAT) in the North America sector. After ~09 UT on 23 June 2015 (Figure 4t), only rather weak auroral irregularities were registered in the American sector. We should note that for both the European and American regions the full picture with the ionospheric irregularities distribution is limited due to an absence of GNSS stations in Africa and the Pacific Ocean, respectively.

4.3. Parameters of the Ionospheric Irregularities Estimated by the COSMIC RO Back Propagation

Figure 5 shows results of localization of the plasma irregularities along the line-of-sight GPS-LEO (COSMIC). Figure 5a shows the propagation geometry. The coordinates of the GPS and LEO satellites

were transformed so that virtual GPS became stationary; the BP plane was set to vertical and the virtual LEO observational trajectory was projected in that plane (more details about this coordinate transformation can be found in Sokolovskiy et al., 2002). The Y coordinate is the distance along the line GPS-LEO in the BP plane, counted from the tangent point (TP) at 80-km height. The Z coordinate is perpendicular to Y and is counted from the surface. Figures 5b–5d represent four COSMIC neutral atmospheric occultations sampled at 50 Hz, collected during the geomagnetic storm. The occultations were selected based on "localizability" of irregularities. Vertical fluctuating lines have a dual sense. First, their Y coordinates denote locations (distances) of the set of the BP planes (to which electromagnetic field was propagated from LEO orbit). Second, their shapes denote normed fluctuations of the BP amplitude along the Z direction at those Y coordinates (normalization was applied for visualization purposes only and it does not matter for the localization).

Besides the scintillations induced by irregularities in the F layer, occultations in Figures 5b and 5e show clearly pronounced scintillations induced by the sporadic E layer at Z around 90–100 km. Blue lines show normed RMS of amplitude fluctuations calculated in Z intervals 85–95 km (Figure 5b) and 95–105 km (Figure 5e) and have clear minima close to $Y = 0$ km, that is, at TP, as this should be for the sporadic E layer (this fact may also be considered an implicit verification of BP). Red lines show RMS of amplitude fluctuations calculated in Z intervals with the excluded sporadic E. They show minima at $Y = 2{,}000$–$2{,}600$ km, that is, far away from TP thus indicating that irregularities are located in the F layer (geographic coordinates and approximate heights of the irregularities are indicated in the figure caption).

4.4. The Ionospheric Plasma Depletions and Irregularities as Specified by In Situ and COSMIC RO Observations

Figure 6 presents an overview of the storm-induced ionospheric irregularities as detected by in situ plasma density observations onboard the Swarm and C/NOFS satellites on 22–23 June 2015. Areas with plasma bite-outs and further development of EPBs are highlighted by a yellow-shaded area for the event #1 in the African sector, by the green area for the event #2 in the American sector.

The tandem of SWA and SWC satellites entered the eastern part (~40°E) of the African sector at ~20 UT on 22 June 2015 (Figure 6c, pass #1, rightmost graph). Both satellites are separated by ~1.4° in longitude and usually they have very similar results with plasma density measurements. Here, they detected none equatorial ionospheric irregularities and showed only weak irregularities near auroral region and main ionospheric trough at both hemispheres. The next SWA/SWC pass (#2) at 21.5–22.0 UT was near 20°E crossing the African continent and central Europe. Both satellites encountered a plasma bite-out in the form of a huge plasma depletion of ~15–20° width in latitude near the geomagnetic equator and the strong irregular structures at the depletion edges extended toward low latitudes. We note that SWC showed even a broader bite-out and clear differences in irregularities location/magnitude, that can be interpreted by differences between satellite pass and geomagnetic field line/location of EPB initial development and its further drift (e.g., Kil et al., 2016). When ~2 hr later the SWB crossed this region (Figure 6d, pass #2), it still registered the great plasma bite-out at ~515-km altitude.

The next SWA/SWC pass (#3) at 23.0–23.5 UT was crossing the western Africa near 6°W. Both satellites encountered the plasma bite-out near the geomagnetic equator and numerous irregular plasma depletions extended from this zone toward low and middle latitudes of both hemispheres from −30°S to 45°N. The plasma depletion seen near 40–45°N occurred exactly over the strong ionospheric irregularities area detected by the ground-based GNSS observations in the southern Europe (cf. Figure 4f). Two hours later, SWB overpassed this region (Figure 6d, pass #3) and also registered plasma bite-out and developed ionospheric irregularities at low and middle latitudes. At that time, the midlatitude depletion near ~40°N was even more pronounced at ~515-km altitude than that detected previously at ~465 km.

The next SWA/SWC passes (Figure 6c, passes #4 and #5) showed an absence of ionospheric irregularities over 30–50°W longitudes that confirmed a very narrow (longitudinal) localization of the storm-induced irregularities related to the PPEF occurrence in the dusk sector. But, the SWB overpassing later the region near ~27°W (Figure 6d, pass #4) encountered signatures of the midlatitude plasma depletion near 40°N and low-latitude depletion near 15°N; it can be related to a slow westward drift of EPBs that was also found in the ground-based GNSS results. We also observed a hemispheric asymmetry for the African sector with a

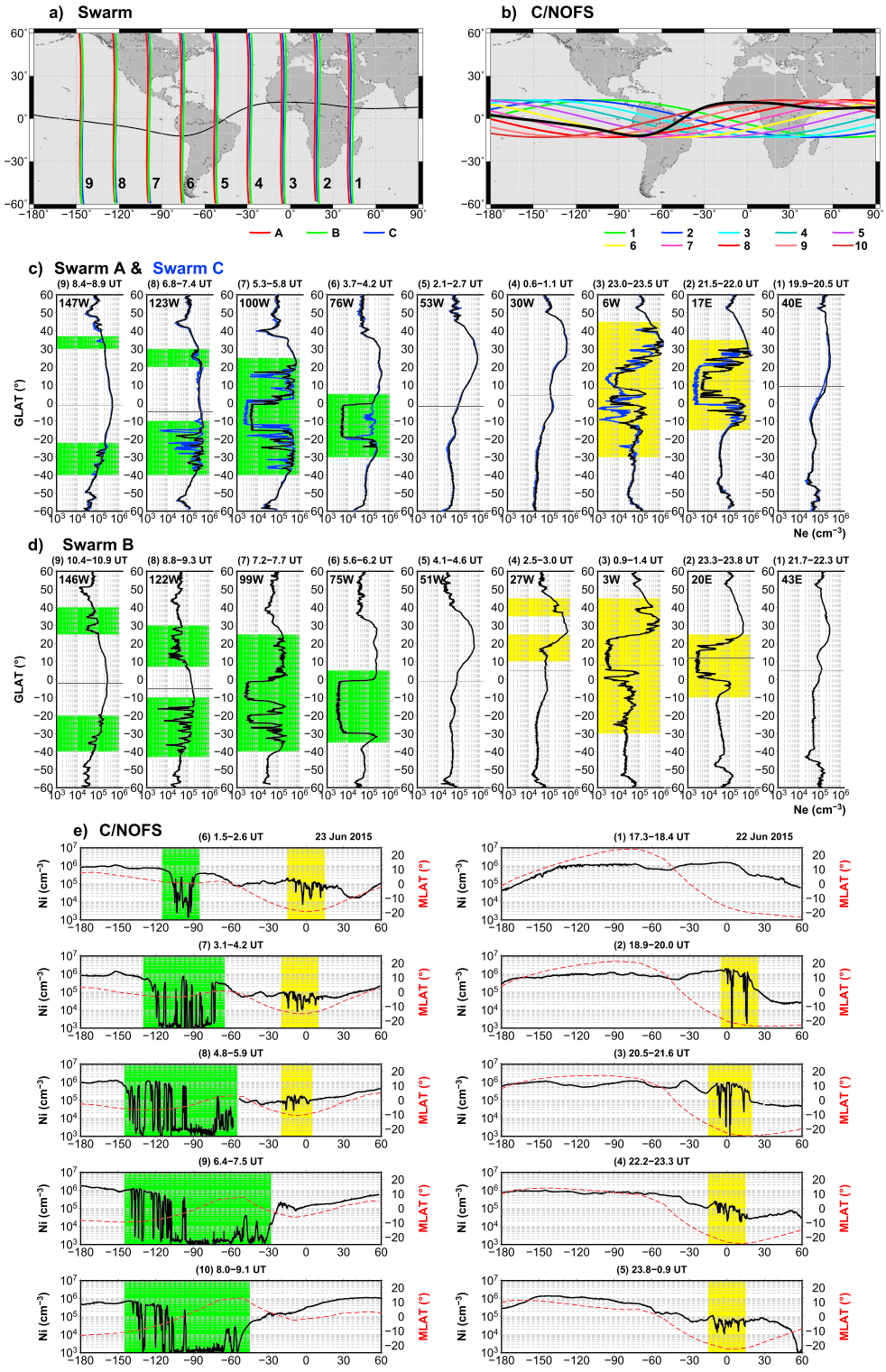

Figure 6. Ionospheric irregularities as detected by in situ plasma density observations onboard Swarm and C/NOFS satellites on 22–23 June 2015. Global map with (a) Swarm satellites passes and (b) C/NOFS passes. Variation of in situ electron density Ne as a function of geographical latitude along (c) tandem passes Swarm A and Swarm C at ~465-km height, (d) Swarm B passes at ~515-km height. Horizontal gray line shows the geomagnetic equator latitude. Graph captions (top) show satellite pass number, UT, and geographic longitude for each pass. (e) Variation of in situ ion density Ni as a function of geographical longitude along C/NOFS passes; red dashed line shows changes in geomagnetic latitude along pass. The yellow and green shadings indicate deep plasma depletions in the African and American sectors, respectively.

significant plasma density enhancement at midlatitudes of the northern (summer) hemisphere during that part of the storm (SWA/SWC/SWB passes #2–#5).

The second event occurred over the American/Pacific sector after two rapid southward IMF Bz turns at ~0:39 UT and at ~01:40 UT on 23 June 2015. When near 04 UT (Figure 6c, pass #6), the tandem first appeared at that region, the SWA detected the new plasma bite-out of ~20° width in latitude near ~76°W. Two hours later (Figure 6d, pass #6), the SWB revealed that this plasma bite-out of over 2 orders of magnitude became even wider (~30° width in latitude) at higher altitudes. The next SWA/SWC pass (Figure 6c, pass #7) crossed the American sector near 100°W at ~5.5 UT; both satellites registered plasma bite-out near the geomagnetic equator and strong plasma irregularities developed toward low and middle latitudes of both hemispheres. Plasma depletions near 15–20°N was collocated with the strong ionospheric irregularities area as detected by the ground-based GNSS observations over central/northern America (cf. Figure 4p and 4q). The main ionospheric trough was registered at much higher latitudes at ~40°N (50° MLAT). Two hours later (Figure 6d, pass #7), the SWB pass encountered plasma bite-out zone and strong ionospheric irregularities prevailing at midlatitudes of the Southern Hemisphere. The next overpasses of SWA/SWC (Figure 6c, pass #8) and SWB (Figure 6d, pass #8) registered (1) no signatures of the plasma bite-out near the geomagnetic equator and (2) moderate-to-strong ionospheric irregularities at low and middle latitudes (up to 30–35° MLAT) mainly at the Southern Hemisphere. We should note that an orientation (eastward tilt) of the geomagnetic field lines over that part of the Pacific Ocean and a slow westward drift of the storm-induced EPBs set the conditions when a satellite with a polar orbit would have a higher chance of detecting these nonequatorial plasma structures over the Southern Hemisphere than over the northern one. Thus, the Swarm observations showed that the storm-induced irregularities were observed over the American sector at least from 03 UT to 10 UT on 23 June 2015. The SWB flying at higher altitudes registered an even larger size of the plasma depletions that became deeper and wider. It can be explained by a gradual evolution of the EPB structures toward the topside ionosphere with time.

Figure 6e shows ion density (Ni) variations along 10 consecutive C/NOFS passes within the equatorial region that substantially complement the Swarm polar overpasses. The C/NOFS orbit was ~330 × 450-km altitude. For the first event in the African sector, the C/NOFS passes were far from the geomagnetic equator, at ~20°S MLAT in the Southern Hemisphere. At ~19:40–19:50 UT, the C/NOFS pass #2 registered two isolated plasma depletions over southern Africa (0–20°E), the satellite was at 380- to 390-km altitude. At that time, at the conjugate hemisphere the ionospheric irregularities have just appeared over southern Europe and northern Africa as was detected by the ground-based GNSS observations. The next pass #3 showed a further development of the southern part of EPBs with a longitudinal increase and a slow westward movement of this zone. The SWA/SWC satellites that appeared later (Figure 6c, pass #2) most probably encountered the rightmost plasma depletion seen near 14°E by C/NOFS. In the southern part of the African sector, the storm-induced irregularities were registered from 19:40 UT on 22 June till 05 UT on 23 June, the zone was slightly drifted westward.

In the American sector, the first signatures of the storm-induced plasma depletions appeared at 01:50–01:55 UT on 23 June 2015 over ~110–88°W; the satellite was just over the geomagnetic equator at ~360- to 370-km altitude (Figure 6e, pass #6). Taking into account time required for EPB generation (~1 hr after sunset) due to PPEF and PRE interaction, we conclude that these EPBs were related to PPEF that occurred after the first IMF Bz turn at ~0:39 UT; at that time the terminator and dusk sector were at ~110–90°W. The C/NOFS pass #7 showed a considerable enlargement of the zone affected by severe plasma depletion in longitudes; at 03–04 UT, it already covered 125–70°W. These broad plasma depletions can be resulted from the PPEF action after the second IMF Bz turn at ~01:40 UT and the prolonged time of the southward Bz. The consecutive C/NOFS passes registered a further great expansion of the zone in longitude with a formation of numerous strong plasma depletions within this zone. According to the C/NOFS observations, the zone affected by the storm-induced EPBs covered 150–30°W and these irregularities were registered from 01:50 UT to at least 10–11 UT on 23 June 2015. The wide plasma bite-outs detected by the Swarm satellites near 75 and 100°W (Figures 6c and 6d, passes #6–7) coincided with the broad plasma depletions seen by the C/NOFS.

The signatures of strong plasma depletions over both considered longitudinal sectors detected practically simultaneously by C/NOFS and Swarm allow us to estimate a spatial/horizontal size of these structures near 400- to 500-km altitude. For the first event in the African sector, the affected area covered 30°S–45°N in

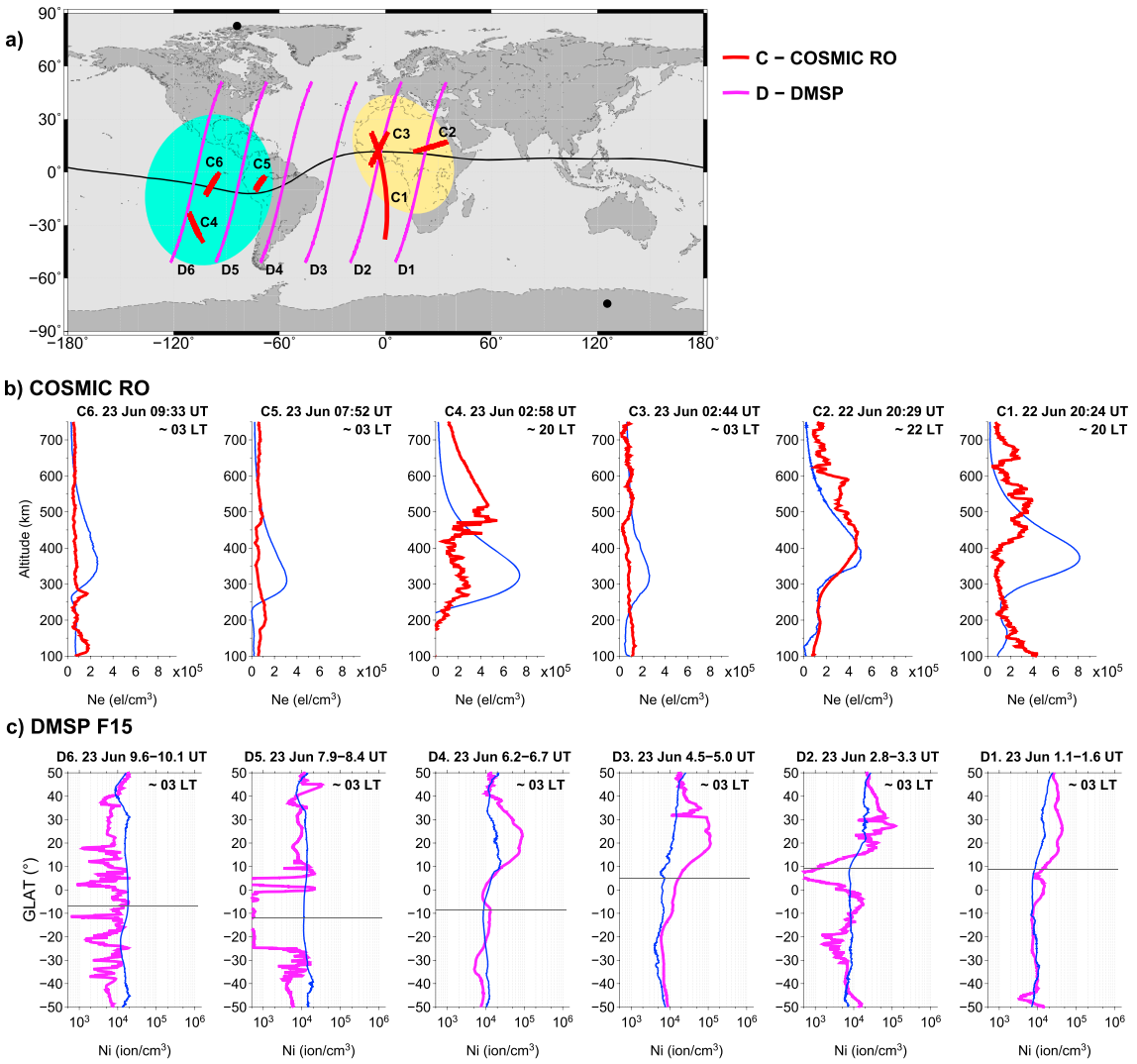

Figure 7. (a) Map with location of six COSMIC RO events and parts of six DMSP passes. (b) COSMIC RO electron density profiles as a function of altitude. (c) Ion density variation as a function of geographical latitude along DMSP F15 passes at ~850-km altitude. Thick color lines show density values for 22–23 June; thin blue lines are quiet-time prestorm conditions of 20–21 June 2015.

latitude and 15°W–20°E in longitude. For the second event in the American sector, the affected area covered 40°S–35°N in latitude and 150–30°W in longitude. From in situ observations, the most dramatic plasma depletions and bite-outs were registered near the geomagnetic equator. The deep plasma density bite-outs indicate that ionospheric plasma was lifted above the Swarm altitude (465–515 km) and was further transported along magnetic field lines. At higher altitudes, the recombination times are much longer (hours) than for lower altitudes, so the ionospheric conditions become more favorable to EPB generation because of the high RTI growth rate.

To analyze the topside ionosphere response (above the F2 layer peak that was more close to the Swarm orbit altitude) and relationships with the plasma irregularities development in the topside ionosphere, we combine COSMIC RO electron density profiles (up to 700 km in altitude) and in situ plasma density measurements onboard the DMSP F15 satellite at ~850-km altitude. Since only three COSMIC satellites operated at that time, a number of RO events occurred at the proper sector/time was rather limited. Figure 7 shows location and electron density profiles for three RO events in the African sector and three RO events in the American sector. The COSMIC RO observations confirm main features of the ionospheric response to the June 2015 storm. In comparison with quiet-time prestorm conditions, shape of RO profiles was significantly distorted by plasma irregularities and gradients at both bottomside and topside parts of profiles. RO events

with a perigee points near the geomagnetic equator (C3, C5, and C6) showed a strong decrease of electron density at all altitudes of RO profile; these measurements corresponded to areas with the plasma bite-outs detected by Swarm and C/NOFS observations (Figure 6).

DMSP in situ plasma density measurements recognized a complex behavior of the topside ionosphere. First pass (D1) showed mainly a plasma density enhancement over the Northern (summer) Hemisphere. The next DMSP pass (D2) crossing Western Africa revealed that even at ~03 UT on 23 June, more than 8 hr after the storm onset, there were still signatures of the plasma bite-out over the magnetic equator with plasma enhancements at both sides of the equator. It means that plasma uplift over Western Africa was above the DMSP orbit of ~850 km. We found that enhancement over 15–45°N latitudes was much larger than the southern one and contained intense plasma structuring with plasma depletions at ~30°N. We note that flatten shape of COSMIC RO profile (Figure 7b, C3) was registered exactly within the plasma bite-out zone seen simultaneously in the D2 pass. The pass (D3) detected plasma density enhancement over the Northern Hemisphere with a clear signature of the plasma depletion at ~30–35°N. Thus, severe plasma density irregularities seen by the ground-based GNSS observations were also registered by the Swarm satellites at ~500-km altitude and by the DMSP satellite at ~850-km altitude. In the American sector, pass (D5) encountered a plasma bite-out near ~85°W and plasma irregularities developed poleward (up to 25° MLAT) from this deep depletion. The C/NOFS observations showed that at that time this bite-out longitude (~85°W) was within broad plasma depletions (Figure 6e, passes #9–10). It indicates that plasma uplift over the American sector was also above the DMSP orbit of ~850 km. The next pass (D6) encountered many intense plasma irregularities over 40°S–20°N (up to 30° MLAT) at that high altitude. The plasma irregularities detected by the ground-based GNSS over central and northern America were recognized as topside plasma depletions by the DMSP data. Joint analysis of the C/NOFS, Swarm, and DMSP observations revealed that these storm-induced EPS structures had extended over 500 km in altitude, at least from ~350 to ~850 km.

We should emphasize that analysis of the storm-induced ionospheric irregularities development on a global scale is a still challenging task, taking into account available data sparsity. Our multi-instrumental and multimission approach bring new knowledge for both the application domain to specify such effects globally (operational ionospheric models and near real-time prediction) and for fundamental tasks of understanding the underlying physics processes.

To investigate the ionospheric response in this case, we try to solve the problem using multi-instrumental observations from several LEOs with a combination of all-available ground-based GNSS observations including GLONASS transionospheric links. The ground-based GPS observations are widely used to study the ionospheric irregularities development at equatorial and polar regions (e.g., Cherniak et al., 2018; Valladares et al., 2004). But, the ground-based GPS/GNSS can provide only two-dimensional projection of plasma structures from all ionospheric altitudes and not always does it allow recognizing the nature of these irregularities. Only combination with other instruments can solve such uncertainties. To estimate an altitudinal distribution of irregularities on a global scale, plasma observation at different LEO orbits is the key solution.

The most interesting results obtained with this approach application were detection of the storm-induced plasma irregularities at low and middle latitudes related to the development of EPBs, whose spatiotemporal pattern and generation mechanisms differed completely from auroral origin ionospheric irregularities developed typically during geomagnetic storms and substorms. Thus, the plasma irregularities that occurred during geomagnetic storms have more complicated drivers and behavior at all locations over the globe. The high-latitude irregularities illustrate a typical reaction of the high-latitude ionosphere to geomagnetic storm/substorm and morphology of these irregularities' occurrence are understood rather well. But due to different processes responsible for such plasma structures generation, complicated dynamics and multiple types of instabilities that occurred within the auroral zone, it is still difficult to predict and nowcast areas and altitudes where strong plasma gradients and irregularities occur, particularly, a degree of an equatorward expansion of the auroral irregularities zone during strong geomagnetic disturbances. Such structures attributed to auroral processes and initiated by energetic particles precipitation from the magnetosphere and by a wide spectrum of plasma instabilities due to the ionosphere/magnetosphere dynamics drivers like subauroral polarization stream electric fields (e.g., Foster & Burke, 2002). For June 2015 geomagnetic storm, intensity of the ionospheric irregularities related with auroral activity was dynamically changed in time.

Initially, the area affected by auroral irregularities was a narrow oval-like structure located poleward 60–65°N MLAT. With the storm development, this zone expanded in size toward ~55°N MLAT at midlatitudes.

The regular appearance of equatorial plasma structures related with postsunset generation mechanism RTI was investigated in detail, including observations, climatology, and numerical simulations (e.g., Huang & Kelley, 1996; Huba & Joyce, 2007, 2010; Ossakow, 1981; Yokoyama et al., 2014). There are several major factors altering the RTI growth rate: PRE of eastward electric field, gravity waves, and meridional wind (Abdu, 2001). Equatorial irregularities are observed predominantly within a region surrounding the geomagnetic equator (±20° MLAT) in quite geomagnetic conditions after sunset. These limits vary depending on LT, location, season, and solar activity. Also, EPBs can be strongly affected by disturbance electric fields, in particular, from PPEF and disturbance dynamo. When the storm-induced electric fields occur in the dusk sector, they can initiate more dramatic EPBs development due to much larger uplift of the ionosphere to high altitudes where the RTI growth rate is maximized (e.g., Abdu et al., 1995; Basu et al., 2001, 2007; Ossakow, 1981). Huang et al. (2007) reported generation of storm-induced EPBs in response to the eastward PPEF occurrence at dusk causing large equatorial plasma uplifts and bite-outs. Huang et al. (2010) discussed effect of the prolonged (~8 hr) eastward PPEF in the dusk sector during long-lasting southward IMF Bz.

For the June 2015 geomagnetic storm, the severe ionospheric irregularities were developed in both the European and American sectors just after the rapid southward turns of IMF Bz. There is a principal difference between both events. The first event in the African sector was initiated by PPEF of relatively short duration, and storm-induced EPBs were rather limited in a longitude range by the corresponding dusk sector (0–20°E). The second event in the American region represents a superposition of EPBs generation in response to multiple PPEF associated with two rapid southward turns of the IMF Bz at ~0:39 UT and at ~01:40 UT on 23 June 2015—the first one was short duration and the second one was long lasting (~4 hr). As a result, the favorable conditions for postsunset EPBs generation in the dusk equatorial ionosphere were maintained for several hours and the storm-induced EPBs were progressively developed over the American/Pacific sector following the sunset terminator—a series of EPBs were generated over a large longitudinal range from 150 to 30°W. The detected EPBs structures were formed in the course of the storm's main phase and persisted over 8 hr. The observed broad plasma depletions can be resulted from merging of multiple EPBs as it was suggested by Huang et al. (2011).

5. Summary

The main results can be summarized as follows:

1. We present an observational evidence that PPEF associated with southward IMF during the geomagnetic storm main phase can induce the large-scale EPBs generation in the postsunset sector even in the precondition of the lowest EPBs occurrence (June solstice).
2. PPEF associated with a long-lasting southward IMF can support favorable conditions for postsunset EPBs generation in the dusk equatorial ionosphere for several hours. As a result, the storm-induced EPBs can be progressively developed over a great longitudinal range following the sunset terminator.
3. The storm-induced large-scale EPBs affected a localized zone of ~20° in the African sector and a large longitudinal range of ~100° in the American sector in response to PPEF events of different duration.
4. Plasma depletions of equatorial origin were registered at midlatitudes (30–40° MLAT) of both hemispheres in the African and American longitudinal sectors.
5. Joint analysis of the COSMIC, C/NOFS, Swarm, and DMSP observations revealed that these storm-induced EPBs structures had extended over 500 km in altitude, at least from ~350 to ~850 km. Plasma bite-outs were seen up to ~850 km by in situ measurements and by COSMIC RO (flatten shape of profiles).
6. From equatorial to midlatitudes, the storm-induced EPBs cause amplitude and phase scintillations of GPS/GNSS signals for ground-based and space-borne (COSMIC RO) measurements. Strong plasma irregularities lead to the EGNOS performance degradation in European midlatitudes. Such storm-induced plasma irregularities at low and middlelatitudes represent an unpredictable and dangerous scenario for navigation-based systems.

The last but not the least result of this study is a demonstration that combination of different ground-based and space-borne observations can allow assessing plasma irregularities parameters in geographical and

altitudinal domain. All these independent multi-instrumental measurements provide a consistent global view on the ionospheric density irregularity distribution and dynamics and allow estimating space weather drivers for plasma irregularities generation. After the end of the C/NOFS mission in 2015, only Swarm provides continuous in situ observations at ionospheric heights near 500 km. Our results confirm a superb potency of the forthcoming COSMIC-2 mission equipped by both in situ plasma probes and GNSS remote sensing payload, including RO instruments. Considering near-equatorial plane of the COSMIC-2 orbit (~24° inclination), this mission will be a valuable source of data for monitoring and deep investigations of the plasma irregularities development and evolution processes in the equatorial and low-latitudinal regions.

Acknowledgments
We acknowledge the UCAR COSMIC Data Analysis and Archive Center for COSMIC RO data (http://cdaac-www.cosmic.ucar.edu/cdaac/products.html), ESA for SWARM data (http://earth.esa.int/swarm), NGDC NOAA for DMSP data (satdat.ngdc.noaa.gov/dmsp/), CDAS services from NASA/Goddard Space Physics Data Facility (R. McGuire) Heliophysics Data Portal for providing C/NOFS CINDI plasma density data (vspo.gsfc.nasa.gov), and NASA/GSFC_x02C8;s Space Physics Data Facility's OMNIWeb service for geophysical parameters data (https://omniweb.gsfc.nasa.gov/ow_min.html). We acknowledge use of raw GNSS data provided by IGS (ftp://cddis.gsfc. nasa.gov), UNAVCO (ftp://data-out.unavco.org), CORS (ftp://geodesy.noaa.gov), SOPAC (ftp://garner.ucsd.edu), EPN (ftp://olggps.oeaw.ac.at), BKGE (ftp://igs.bkg.bund.de/euref/obs), IGN (ftp://rgpdata.ign.fr), SWEPOS (swepos.lantmateriet.se), FGI-FinnRef (eurefin.fgi.fi), NOANET (www.gein.noa.gr), Natural Resources Canada (webapp.geod.nrcan.gc.ca), CHAIN (ftp://chain.physics.unb.ca/gps/), INEGI (ftp://geodesia.inegi.org.mx), RBMC (ftp://geoftp.ibge.gov.br/RBMC/), and RAMSAC CORS of National Geographic Institute of Argentina (www.igm.gov.ar/NuestrasActividades/Geodesia/Ramsac/). The research is supported by the National Science Foundation CAS AGS-1033112, the NASA LWS grant NNX15AB83G, and by the National Science Centre, Poland, through grants 2017/25/B/ST10/00479 and 2017/27/B/ST10/02190.

References

Aa, E., Huang, W., Liu, S., Ridley, A., Zou, S., Shi, L., et al. (2018). Midlatitude plasma bubbles over China and adjacent areas during a magnetic storm on 8 September 2017. *Space Weather*, *16*, 321–331. https://doi.org/10.1002/2017SW001776

Aarons, J. (1991). The role of the ring current in the generation or inhibition of equatorial *F* layer irregularities during magnetic storms. *Radio Science*, *26*(4), 1131–1149. https://doi.org/10.1029/91RS00473

Aarons, J. (1997). Global Positioning System phase fluctuations at auroral latitudes. *Journal of Geophysical Research*, *102*(A8), 17,219–17,231. https://doi.org/10.1029/97JA01118

Abdu, M. A. (2001). Outstanding problems in the equatorial ionosphere–thermosphere electrodynamics relevant to spread *F*. *Journal of Atmospheric and Solar - Terrestrial Physics*, *63*(9), 869–884. https://doi.org/10.1016/S1364-6826(00)00201-7

Abdu, M. A., Batista, I. S., Walker, G. O., Sobral, J. H. A., Trivedi, N. B., & de Paula, E. R. (1995). Equatorial ionospheric fields during magnetospheric disturbances: Local time/longitudinal dependences from recent EITS campaigns. *Journal of Atmospheric and Solar - Terrestrial Physics*, *57*(10), 1065–1083. https://doi.org/10.1016/0021-9169(94)00123-6

Augusto, C. R. A., Navia, C. E., de Oliveira, M. N., Nepomuceno, A. A., Raulin, J. P., Tueros, E., et al. (2018). The 2015 summer solstice storm: One of the major geomagnetic storms of solar cycle 24 observed at ground level. *Solar Physics*, *293*(5). https://doi.org/10.1007/s11207-018-1303-8

Basu, S., & Basu, S. (1989). Scintillation technique for probing ionospheric irregularities. In *World ionosphere/thermosphere studies, WITS handbook*, (pp. 128–136). Urbana: SCOSTEP, Univ. of Ill.

Basu, S., Basu, S., Groves, K. M., Yeh, H. C., Su, S. Y., Rich, F. J., et al. (2001). Response of the equatorial ionosphere in the South Atlantic region to the great magnetic storm of July 15, 2000. *Geophysical Research Letters*, *28*(18), 3577–3580. https://doi.org/10.1029/2001GL013259

Basu, S., Basu, S., Groves, K. M., Mackenzie, E., Keskinen, M. J., & Rich, F. J. (2005). Near-simultaneous plasma structuring in the mid-latitude and equatorial ionosphere during magnetic superstorms. *Geophysical Research Letters*, *32*, L12S05. https://doi.org/10.1029/2004GL021678

Basu, S., Basu, S., Rich, F. J., Groves, K. M., MacKenzie, E., Coker, C., et al. (2007). Response of the equatorial ionosphere at dusk to penetration electric fields during intense magnetic storms. *Journal of Geophysical Research*, *112*, A08308. https://doi.org/10.1029/2006JA012192

Basu, S., Basu, S., & Khan, B. K. (1976). Model of equatorial scintillations from in-situ measurements. *Radio Science*, *11*(10), 821–832. https://doi.org/10.1029/RS011i010p00821

Basu, S., Basu, S., Makela, J. J., Mackenzie, E., Doherty, P., Wright, J. W., et al. (2008). Large magnetic storm-induced nighttime ionospheric flows at midlatitudes and their impacts on GPS-based navigation systems. *Journal of Geophysical Research*, *113*, A00A06. https://doi.org/10.1029/2008JA013076

Burke, W. J., Huang, C. Y., Valladares, C. E., & Su, S.-Y. (2004). Longitudinal variability of equatorial plasma bubbles observed by DMSP and ROCSAT-1. *Journal of Geophysical Research*, *109*, A12301. https://doi.org/10.1029/2004JA010583

Cherniak, I., Krankowski, A., & Zakharenkova, I. (2014). Observation of the ionospheric irregularities over the Northern Hemisphere: Methodology and service. *Radio Science*, *49*, 653–662. https://doi.org/10.1002/2014RS005433

Cherniak, I., Krankowski, A., & Zakharenkova, I. (2018). ROTI maps: A new IGS ionospheric product characterizing the ionospheric irregularities occurrence. *GPS Solutions*, *22*(3). https://doi.org/10.1007/s10291-018-0730-1

Cherniak, I., & Zakharenkova, I. (2016). First observations of super plasma bubbles in Europe. *Geophysical Research Letters*, *43*, 11,137–11,145. https://doi.org/10.1002/2016GL071421

Cherniak, I., & Zakharenkova, I. (2017). New advantages of the combined GPS and GLONASS observations for high-latitude ionospheric irregularities monitoring: Case study of June 2015 geomagnetic storm. *Earth, Planets and Space*, *69*(1). https://doi.org/10.1186/s40623-017-0652-0

Cherniak, I., Zakharenkova, I., & Redmon, R. J. (2015). Dynamics of the high-latitude ionospheric irregularities during the 17 March 2015 St. Patrick's Day storm: Ground-based GPS measurements. *Space Weather*, *13*, 585–597. https://doi.org/10.1002/2015SW001237

Doherty, P., Coster, A. J., & Murtagh, W. (2004). Eye on the ionosphere: Space weather effects of October-November 2003. *GPS Solutions*, *8*(4), 267–271. https://doi.org/10.1007/s10291-004-0109-3

Fejer, B. G., Scherliess, L., & de Paula, E. R. (1999). Effects of the vertical plasma drift velocity on the generation and evolution of equatorial spread *F*. *Journal of Geophysical Research*, *104*(A9), 19,859–19,869. https://doi.org/10.1029/1999JA900271

Foster, J. C., & Burke, W. J. (2002). SAPS: A new categorization for sub-auroral electric fields. *Eos*, *83*(36), 393–394. https://doi.org/10.1029/2002EO000289

Gorbunov, M. E., Gurvich, A. S., & Shmakov, A. V. (2002). Back-propagation and radio-holographic methods for investigation of sporadic ionospheric *E*-layers from Microlab-1 data. *International Journal of Remote Sensing*, *23*(4), 675–685. https://doi.org/10.1080/01431160010030091

Hinson, D. P., Twicken, J. D., & Karayel, E. T. (1998). Jupiter's ionosphere: New results from Voyadger 2 radio occultation measurements. *Journal of Geophysical Research*, *103*(A5), 9505–9520. https://doi.org/10.1029/97JA03689

Huang, C.-S., de La Beaujardiere, O., Roddy, P. A., Hunton, D. E., Pfaff, R. F., Valladares, C. E., & Ballenthin, J. O. (2011). Evolution of equatorial ionospheric plasma bubbles and formation of broad plasma depletions measured by the C/NOFS satellite during deep solar minimum. *Journal of Geophysical Research*, *116*, A03309. https://doi.org/10.1029/2010JA015982

Huang, C.-S., Foster, J. C., & Sahai, Y. (2007). Significant depletions of the ionospheric plasma density at middle latitudes: A possible signature of equatorial spread *F* bubbles near the plasmapause. *Journal of Geophysical Research*, *112*, A05315. https://doi.org/10.1029/2007JA012307

Huang, C.-S., & Kelley, M. C. (1996). Nonlinear evolution of equatorial spread *F*: 2. Gravity wave seeding of Rayleigh-Taylor instability. *Journal of Geophysical Research*, *101*(A1), 293–302. https://doi.org/10.1029/95JA02210

Huang, C. S., Rich, F. J., & Burke, W. J. (2010). Storm time electric fields in the equatorial ionosphere observed near the dusk meridian. *Journal of Geophysical Research*, *115*, A08313. https://doi.org/10.1029/2009JA015150

Huba, J. D., & Joyce, G. (2007). Equatorial spread *F* modeling: Multiple bifurcated structures, secondary instabilities, large density "bite-outs," and supersonic flows. *Geophysical Research Letters*, *34*, L07105. https://doi.org/10.1029/2006GL028519

Huba, J. D., & Joyce, G. (2010). Global modeling of equatorial plasma bubbles. *Geophysical Research Letters*, *37*, L17104. https://doi.org/10.1029/2010GL044281

Jakowski, N., Béniguel, Y., De Franceschi, G., Hernández-Pajares, M., Jacobsen, K. S., Stanislawska, I., et al. (2012). Monitoring, tracking and forecasting ionospheric perturbations using GNSS techniques. *Journal of Space Weather and Space Climate*, *2*, A22. https://doi.org/10.1051/swsc/2012022

Jakowski, N., Mielich, J., Borries, C., Cander, L., Krankowski, A., Nava, B., & Stankov, S. M. M. (2008). Large-scale ionospheric gradients over Europe observed in October 2003. *Journal of Atmospheric and Solar-Terrestrial Physics*, *70*(15), 1894–1903. https://doi.org/10.1016/j.jastp.2008.03.020

Jiao, Y., Morton, Y. T., Taylor, S., & Pelgrum, W. (2013). Characterization of high-latitude ionospheric scintillation of GPS signals. *Radio Science*, *48*, 698–708. https://doi.org/10.1002/2013RS005259

Kelley, M. (1989). *The Earth's ionosphere*, (p. 487). San Diego: Academic Press.

Kil, H., Lee, W. K., Paxton, L. J., Hairston, M. R., & Jee, G. (2016). Equatorial broad plasma depletions associated with the evening pre-reversal enhancement and plasma bubbles during the 17 March 2015 storm. *Journal of Geophysical Research: Space Physics*, *121*, 10,209–10,219. https://doi.org/10.1002/2016JA023335

Ma, G., & Maruyama, T. (2006). A super bubble detected by dense GPS network at east Asian longitudes. *Geophysical Research Letters*, *33*, L21103. https://doi.org/10.1029/2006GL027512

NOAA Space Weather Highlights. 2019. SWPC PRF 2078. ftp://ftp.swpc.noaa.gov/pub/warehouse/2018/WeeklyPDF/prf2078.pdf. Accessed 22 January 2019.

Ossakow, S. L. (1981). Spread *F* theories: A review. *Journal of Atmospheric and Terrestrial Physics*, *43*(5-6), 437–452. https://doi.org/10.1016/0021-9169(81)90107-0

Pi, X., Mannucci, A. J., Lindqwister, U. J., & Ho, C. M. (1997). Monitoring of global ionospheric irregularities using the worldwide GPS network. *Geophysical Research Letters*, *24*(18), 2283–2286. https://doi.org/10.1029/97GL02273

Prikryl, P., Jayachandran, P. T., Mushini, S. C., Pokhotelov, D., MacDougall, J. W., Donovan, E., et al. (2010). GPS TEC, scintillation and cycle slips observed at high latitudes during solar minimum. *Annales Geophysicae*, *28*(6), 1307–1316. https://doi.org/10.5194/angeo-28-1307-2010

Reiff, P. H., Daou, A. G., Sazykin, S. Y., Nakamura, R., Hairston, M. R., Coffey, V., et al. (2016). Multispacecraft observations and modeling of the 22/23 June 2015 geomagnetic storm. *Geophysical Research Letters*, *43*, 7311–7318. https://doi.org/10.1002/2016GL069154

Roy, B., DasGupta, A., & Paul, A. (2013). Impact of space weather events on satellite-based navigation. *Space Weather*, *11*, 680–686. https://doi.org/10.1002/2013SW001001

Shagimuratov, I. I., Krankowski, A., Ephishov, I., Cherniak, Y., Wielgosz, P., & Zakharenkova, I. (2012). High latitude TEC fluctuations and irregularity oval during geomagnetic storms. *Earth, Planets and Space*, *64*(6), 521–529. https://doi.org/10.5047/eps.2011.10.015

Skone, S., Feng, M., Ghafoori, F., & Tiwari, R. (2008). Investigation of scintillation characteristics for high latitude phenomena. In: *Proceedings of the 21st International Technical Meeting of the Satellite Division of The Institute of* Navigation *(ION GNSS 2008)*, Savannah, GA, September 2008, 2425–2433.

Sokolovskiy, S., Schreiner, W., Rocken, C., & Hunt, D. (2002). Detection of high-altitude ionospheric irregularities with GPS/MET. *Geophysical Research Letters*, *29*(3), 1033. https://doi.org/10.1029/2001GL013398

Valladares, C. E., Villalobos, J., Sheehan, R., & Hagan, M. P. (2004). Latitudinal extension of low-latitude scintillations measured with a network of GPS receivers. *Annales Geophysicae*, *22*(9), 3155–3175. https://doi.org/10.5194/angeo-22-3155-2004

Woodman, R., & La Hoz, C. (1976). Radar observations of *F* region equatorial irregularities. *Journal of Geophysical Research*, *81*(31), 5447–5466. https://doi.org/10.1029/JA081i031p05447

Yokoyama, T., Shinagawa, H., & Jin, H. (2014). Nonlinear growth, bifurcation, and pinching of equatorial plasma bubble simulated by three-dimensional high-resolution bubble model. *Journal of Geophysical Research: Space Physics*, *119*, 10,474–10,482. https://doi.org/10.1002/2014JA020708

Zakharenkova, I., Astafyeva, E., & Cherniak, I. (2016a). GPS and GLONASS observations of large-scale traveling ionospheric disturbances during the 2015 St. Patrick's day storm. *Journal of Geophysical Research: Space Physics*, *121*, 12,138–12,156. https://doi.org/10.1002/2016JA023332

Zakharenkova, I., Astafyeva, E., & Cherniak, I. (2016b). GPS and in situ Swarm observations of the equatorial plasma density irregularities in the topside ionosphere. *Earth, Planets and Space*, *68*, 120. https://doi.org/10.1186/s40623-016-0490-5